Table 1. Orbital elements for six small satellites of Saturn; epoch 244 4513.5 (1 October 1980, 0 hours Ephemeris Time).

| Parameter* | 1980S1 | 1980S3 | 1980S6 | 1980S26 | 1980S27 | 1980S28 |
|---|---|---|---|---|---|---|
| $a$† | 1.51472 × $10^5$ | 1.51422 × $10^5$ | 3.7806 × $10^5$ | 1.41700 × $10^5$ | 1.39353 × $10^5$ | 1.37670 × $10^5$ |
| $e$ | .007 ± .002 | .009 ± .002 | .005 ± .003 | .004 ± .003 | .003 ± .003 | .002 ± .003 |
| $i$ | 0.14° ± 0.05° | 0.34° ± 0.05° | 0.15° ± 0.2° | 0.05° ± 0.15° | 0.0° ± 0.15° | 0.3° ± 0.2° |
| $\tilde{\omega}$‡ | 82° ± 12° | 193° ± 10° | | | | |
| $\Omega$‡ | 87° ± 30° | 134° ± 10° | | | | |
| $\lambda$ | 138.24° ± 0.2° | 21.2° ± 0.2° | 150.75° ± 0.1° | 52.1° ± 0.5° | 109.0° ± 0.5° | 252.0° ± 1.5° |
| $n$ | 518.236 ± 0.01 | 518.490 ± 0.01 | 131.43 ± 0.02 | 572.77 ± 0.02 | 587.28 ± 0.02 | 598.08 ± 0.05 |

* Symbols: $a$, semimajor axis; $e$, eccentricity; $\lambda$, longitude at epoch; $n$, mean motion (degrees per day). Other symbols are defined in the text. † Computed by using $n$ and $J_2$ (*9*); uncertainties in $a$ are essentially represented by the error in $n$. ‡ The errors in these parameters for 1980S6, 1980S26, 1980S27, and 1980S28 are currently so large as to make the values essentially meaningless.

where $\Omega$ is the angle (at epoch) to the orbit's ascending node on Saturn's equator and $\tilde{\omega}$ is the longitude of periapse (also at epoch), both measured from Saturn's autumnal equinox, and $i$ is the inclination. The longitude at epoch is also referred to the autumnal equinox.

The dynamic model for all satellites is a Keplerian ellipse whose apse and node precess under the influences of the central-body harmonics. No attempt was made to model resonance libration terms. The pole and the gravitational harmonics $J_2$ and $J_4$ of Saturn are from (*9*). In computing the nodal and apsidal rates it was assumed that the dominant effects were due to $J_2$ and $J_4$.

The uncertainty associated with each parameter is an estimate of the real error, not merely a formal statistic. Over the observing interval, the camera resolution increased from ~ 900 km per pixel (*10*) 75 days from Saturn to ~ 50 km per pixel in the last pictures taken 3 days before encounter. In general, the root-mean-square (RMS) fit was ~ 0.5 pixel over each satellite's recorded interval, except for 1980S28, for which the eight observations over 6 days were fit to ~ 1 pixel RMS. Approximately 20 observations were used for both 1980S26 and 1980S27, and 40 for both 1980S1 and 1980S3.

In evaluating eccentricity and inclination, the largest source of error is the difficulty of making useful measurements when the satellites are in transit or approaching transit. At these times, particularly for 1980S26, 1980S27, and 1980S28, it is difficult to separate the image of the satellite from the heavily exposed image of the bright rings; with further processing, we hope to be able to include such data in future analyses.

The orbital elements for the six satellites are given in Table 1. It should be noted that these elements are for osculating orbits at the epoch of the observations. This is especially important when considering 1980S1 and 1980S3, which periodically exchange orbits (*11*), and 1980S6, which moves about the leading triangular libration point of Dione.

Satellites 1980S26 and 1980S27 are the outer and inner "shepherding" satellites that stabilize Saturn's F ring (*3*). We call attention to the fact that 1980S26 is itself stabilized by a 3:2 resonance with Mimas, which prevents the satellite–ring particle interaction from forcing 1980S26 outward.

S. P. SYNNOTT
C. F. PETERS
*Jet Propulsion Laboratory, Pasadena, California 91103*
B. A. SMITH
*Department of Planetary Sciences, University of Arizona, Tucson 85721*
L. A. MORABITO
*Jet Propulsion Laboratory*

**References and Notes**

1. H. J. Reitsema, B. A. Smith, S. M. Larson, *Icarus* **43**, 116 (1980).
2. J. W. Fountain and S. M. Larson, *ibid.* **36**, 92 (1978).
3. J. Lechacheux *et al.*, *ibid.* **43**, 115 (1980).
4. A. Dollfus, *Astronomie* **6**, 253 (1968).
5. B. A. Smith *et al.*, *Science* **212**, 163 (1981).
6. These are temporary designations adopted by the International Astronomical Union for new or unidentified satellites. Thus 1980S3 is the third unidentified satellite observed in 1980. Permanent names will eventually be assigned.
7. Private communication.
8. D. Brouwer and G. M. Clemence, *Methods of Celestial Mechanics* (Academic Press, New York, 1961).
9. G. W. Null, E. Lau, E. Biller, J. D. Anderson, *Astron. J.*, in press.
10. A single resolution element on the Voyager images is referred to as a pixel.
11. B. A. Smith *et al.*, in preparation.
12. We wish to thank A. J. Donegan for extensive computing support. This report represents the results of one phase of research carried out at the Jet Propulsion Laboratory, California Institute of Technology, under NASA contract NAS 7-100.

9 February 1981

## Infrared Observations of the Saturnian System from Voyager 1

Abstract. *During the passage of Voyager 1 through the Saturn system, the infrared instrument acquired spectral and radiometric data on Saturn, the rings, and Titan and other satellites. Infrared spectra of Saturn indicate the presence of $H_2$, $CH_4$, $NH_3$, $PH_3$, $C_2H_2$, $C_2H_6$, and possibly $C_3H_4$ and $C_3H_8$. A hydrogen mole fraction of 0.94 is inferred with an uncertainty of a few percent, implying a depletion of helium in the atmosphere of Saturn relative to that of Jupiter. The atmospheric thermal structure of Saturn shows hemisphere asymmetries that are consistent with a response to the seasonally varying insolation. Extensive small-scale latitudinal structure is also observed. On Titan, positive identifications of infrared spectral features are made for $CH_4$, $C_2H_2$, $C_2H_4$, $C_2H_6$, and HCN; tentative identifications are made for $C_3H_4$ and $C_3H_8$. The infrared continuum opacity on Titan appears to be quite small between 500 and 600 $cm^{-1}$, implying that the solid surface is a major contributor to the observed emission over this spectral range; between 500 and 200 $cm^{-1}$ the opacity increases with decreasing wave number, attaining an optical thickness in excess of 2 at 200 $cm^{-1}$. Temperatures near the 1-millibar level are independent of longitude and local time but show a decrease of ~ 20 K between the equator and north pole, which suggests a seasonally dependent cyclostrophic zonal flow in the stratosphere of ~ 100 meters per second. Measurements of the C ring of Saturn yield a temperature of 85 ± 1 K and an infrared optical depth of 0.09 ± 0.01. Radiometer observations of sunlight transmitted through the ring system indicate an optical depth of $10^{-1.3\ \pm 0.3}$ for the Cassini division. A phase integral of 1.02 ± 0.06 is inferred for Rhea, which agrees with values for other icy bodies in the solar system. Rhea eclipse observations indicate the presence of surface materials with both high and low thermal inertias, the former most likely a blocky component and the latter a frost.*


0036-8075/81/0410-0192$02.00/0 

As Voyager 1 passed through the Saturnian system, the infrared instrument (IRIS) obtained a large number of spectra and radiometric data from Saturn, the rings, and Titan and several other satellites. IRIS consists of a Michelson interferometer, which records the spectrum between approximately 180 and 2500 $cm^{-1}$ with a resolution of 4.3 $cm^{-1}$, and a single-channel radiometer, which operates in the visible and near-infrared (*1*). The common 0.25° field of view of the interferometer and the radiometer is boresighted with the fields of other instruments on the Voyager scan platform. IRIS maintained its sensitivity during the 21-month journey from Jupiter and performed well during the Saturn encounter.

Results of the infrared investigation from the Jovian encounters have been published (*2*). This report presents preliminary results on the Saturnian system obtained by the Voyager infrared investigation. The composition, thermal structure, and dynamics of the atmospheres of Saturn and Titan are examined and the properties of the rings of Saturn and Rhea are discussed.

*Saturn.* About 3 weeks before closest approach, the angular diameter of Saturn equaled the IRIS field of view, but only within 8 days of encounter was Saturn sufficiently large to fill the field without interference from the rings and deep space. At closest approach the IRIS field was less than 1/150 of the apparent diameter of Saturn.

In Fig. 1 two infrared emission spectra of Saturn are compared with a Jovian spectrum and a calculated spectrum of Saturn. Spectrum *a*, an average of 51 individual Jovian spectra from the clearest region of the North Equatorial Belt, was recorded by Voyager 1 in March 1979. Spectrum *b* is an average of 791 individual Saturnian spectra, all recorded within 2 days of closest approach, with emission angles of less than 45° and from two latitude bands between 15° and 50° north and south. Spectrum *c* has been synthesized by a radiative transfer program, which uses the vertical temperature profile derived from the measured mid-latitude spectrum and molecular parameters of a mixture of $H_2$, He, $PH_3$, $NH_3$, $CH_4$, $C_2H_2$, and $C_2H_6$ in the abundances listed in Table 1. Spectrum *d* is an average of 43 spectra recorded near the south pole of Saturn at an emission angle of 76°.

As expected, the brightness temperatures of the mid-latitude spectrum of Saturn are 30 to 40 K lower than those of Jupiter. In both cases the $S_0$ and $S_1$ lines of molecular hydrogen are evident at 350 and 600 $cm^{-1}$, respectively, but the detailed line shapes differ on the two planets, partly because of different vertical temperature profiles and emission angles and partly because of different He and $NH_3$ concentrations. In the south polar spectrum the extremely high emission angle shifts the weighting functions of the hydrogen lines to near and above the atmospheric temperature minimum and causes the line centers to appear in emission.

Table 1. Atmospheric composition of Saturn.

| Gas | Band | Wave number ($cm^{-1}$) | Approximate mole fraction |
|---|---|---|---|
| Positively identified | | | |
| Hydrogen ($H_2$) | $S_0$, $S_1$ | 300 to 700 | 0.94 |
| Helium (He) | | 200 to 600 | 0.06 |
| Ammonia ($NH_3$) | Rotational | ~ 200 | $2 \times 10^{-4}$* |
| Phosphine ($PH_3$) | $\upsilon_2$ | 990 | $1 \times 10^{-6}$ |
| Methane ($CH_4$) | $\upsilon_4$ | 1304 | $8 \times 10^{-4}$* |
| Ethane ($C_2H_6$) | $\upsilon_9$ | 821 | $5 \times 10^{-6}$ |
| Acetylene ($C_2H_2$) | $\upsilon_5$ | 729 | $2 \times 10^{-8}$ |
| Tentatively identified | | | |
| Methylacetylene ($C_3H_4$) | $\upsilon_9$ | 633 | |
| Propane ($C_3H_8$) | $\upsilon_{26}$ | 748 | |

*Assumed value.

The spectral features of tropospheric $NH_3$, so prominent in the Jovian spectrum shown in Fig. 1, are weak on Saturn, where $NH_3$ is strongly depleted by condensation in the upper troposphere as a consequence of low temperatures. With the reduced $NH_3$ concentration the 1000-$cm^{-1}$ region of Saturn is dominated by spectral features of $PH_3$ rather than $NH_3$, as on Jupiter. On both planets emission by stratospheric $CH_4$ and its photochemical derivatives $C_2H_2$ and $C_2H_6$ is apparent. The concentrations of these gases are approximately the same in both atmospheres and the differences in appearance of the spectral features are primarily caused by differences in the pressure scale height and the vertical temperature gradient. The high emission angle of the south polar spectrum emphasizes spectral features of stratospheric constituents. In addition to the well-known features (*3*) identified in the mid-latitude spectrum, weak indications of the presence of methylacetylene ($C_3H_4$) and propane ($C_3H_8$) are seen at 633 and 748 $cm^{-1}$, respectively (Fig. 2). Further analysis will be necessary to confirm these identifications. Molecular constituents thus far identified in the Saturn spectra are listed in Table 1.

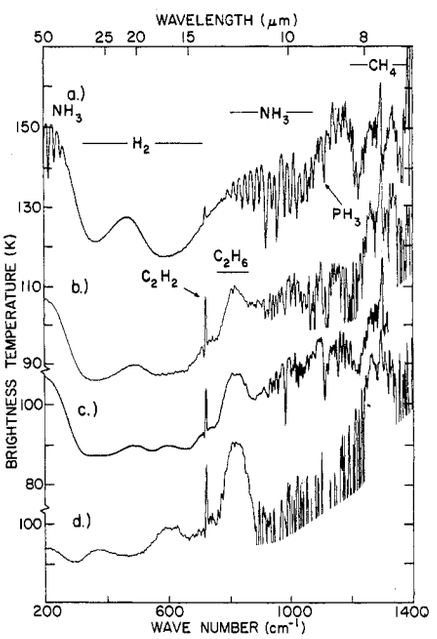


Fig. 1. Saturn spectra and comparison spectra. (a) Spectrum of the North Equatorial Belt of Jupiter recorded by Voyager 1 IRIS in March 1979. (b) Large average of Saturn spectra taken between 15° and 50° north and south. (c) Synthesized Saturn spectrum using only molecular absorption and a mid-latitude temperature profile. (d) South polar spectrum of Saturn recorded at an emission angle of 76°.

The radiative transfer inversion methods of Gautier and colleagues (*4*, *5*), which were used to derive the hydrogen and helium abundances of Jupiter, were also applied to Saturn. The Saturn data differ from those of Jupiter in several significant respects. First, because the low temperatures on Saturn cause strong depletion of $NH_3$ in the atmospheric layers sensed by IRIS, measurements between 200 and 280 $cm^{-1}$ can be used in the Saturn analysis. This spectral region, which could not be used in the Jovian determination, is most sensitive to the helium abundance, as illustrated in figure 2 of Gautier *et al.* (*5*). Second, because the brightness temperatures on Saturn are lower than those on Jupiter (Fig. 1), averaging of Saturn spectra is necessary to ensure that errors due to random instrument noise are smaller than errors from other sources. For the Saturn anal-

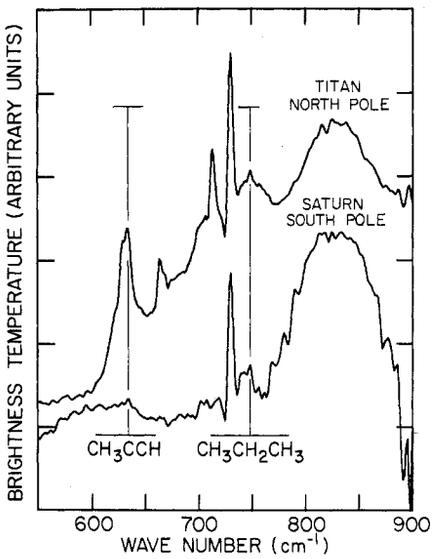


Fig. 2. Tentative identification of $C_3H_4$ and $C_3H_8$ features on Saturn and Titan. The upper spectrum is an average of 72 spectra of the north polar region of Titan, while the lower spectrum is an average of 62 spectra from the south polar region of Saturn. Only relative brightness temperatures are shown since both data sets contain spectra not fully on the disk.

ysis, sets of about 25 spectra each were selected from homogeneous regions at nearly identical latitudes and emission angles. Only sets with a standard deviation approaching the noise-equivalent spectral radiance (*1*) were used. Third, although some areas of Saturn display brightness temperatures in the 2000-$cm^{-1}$ atmospheric window as high as ~ 210 K, the pronounced "hot spots" (~ 260 K) seen on Jupiter and associated with relatively cloud-free regions are absent. Therefore, the possible effect of haze and clouds on the spectral radiances is difficult to evaluate. The good agreement between measured spectra and spectra computed with only molecular constituents suggests that the influence of particulates is small, but a more thorough analysis is required before a definitive statement on the effect of aerosols can be made.

The wave numbers 207, 245, 270, 304.5, 330, 355, 475, 530, and 602 $cm^{-1}$ have been chosen for analysis of the hydrogen and helium abundances. The lowest wave numbers have been selected to fall between the weak $NH_3$ lines. At and above 260 $cm^{-1}$, a polynominal fitting was applied to spectral intervals 20 to 40 $cm^{-1}$ wide. This lowers the spectral resolution and improves the signal-to-noise ratios. Averages of sets of 25 spectra selected for six different latitudes in the southern hemisphere were analyzed to yield values of the hydrogen mole fraction $q$. No systematic dependence of $q$ on latitude or emission angle was found. A mean value of $q = 0.940 \pm 0.005$ was obtained. The standard error reflects only the effects of random noise in the instrument, pointing uncertainties, and variability due to atmospheric conditions.

Other systematic errors have not yet been fully evaluated. However, contrary to the Jovian case, errors caused by uncertainties in the hydrogen and helium absorption coefficients are relatively small on Saturn because the lowest useful wave number, 207 $cm^{-1}$, falls in a region where the pressure-induced $H_2$-He absorption coefficients are larger than the $H_2$-$H_2$ coefficients (*5*). A 5 percent uncertainty in the knowledge of the absorption coefficients translates into an uncertainty in $q$ of only $\pm$ 0.005. Another potential source of error concerns assumptions at the lower boundary of the atmospheric layers under investigation. At levels deeper than about 700 mbar, contributions to the measured radiances decrease rapidly, and no direct information on the temperature structure can be retrieved. However, these small contributions must be included in the analysis, and for this reason the temperature profiles are extrapolated along adiabats below the 700-mbar level. This extrapolation is based on the assumption that the vertical energy flux will be carried by convection at deep levels. However, it is not certain that the adiabatic lapse rate actually begins at the 700-mbar level. Since the results are somewhat sensitive to the assumed level, errors can result from an incorrect choice. Neither this effect nor other systematic effects have been sufficiently investigated to obtain a realistic error estimate. However, the uncertainty in $q$ is at least 0.01, but probably not more than 0.03. The derived $q$ may therefore be compatible with the value 0.90 $\pm$ 0.03 derived from Pioneer data (*6*), especially since the latter error estimate does not include systematic effects other than those of the Pioneer radiometer.

Ignoring the effect of heavy elements, the present best value of $q$, 0.94, yields a helium mass fraction of $Y = 0.11$, again with an error of a few percent. This is less than the value $Y = 0.19 \pm 0.05$ previously obtained for Jupiter by the same analysis technique (*5*). As discussed by Stevenson and Salpeter (*7*) and Stevenson (*8*), an atmospheric depletion of this magnitude implies significant gravitational separation of helium and hydrogen in Saturn's interior. This is consistent with energy balance considerations. Homogeneous models of the interior, which

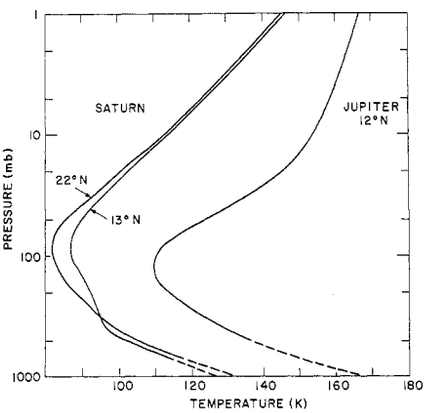


Fig. 3. Vertical temperature profiles for Saturn and Jupiter, as retrieved by inversion of Voyager IRIS spectra. The dashed portions of the curves represent extrapolations along adiabats.

do not allow for differentiation, predict a decay in luminosity to the present value in only $2 \times 10^9$ years—less than the presumed age of the solar system, $4.5 \times 10^9$ years (*9*). Our measurement, $\Delta Y \simeq 0.08$, implies an energy release of $\sim 10^{41}$ ergs (*10*), which could sustain Saturn's current internal luminosity, $\sim 10^{24}$ erg $sec^{-1}$, for the required additional time. The precise value of the internal luminosity of Saturn has not yet been determined from IRIS data. Preliminary analysis indicates that the IRIS results are approximately consistent with the Pioneer-derived effective emission temperature of ~ 96.5 K (*6*), but that the geometric albedo of 0.36 derived by Harris (*11*) is too high.

The thermal structure of Saturn has been investigated by using radiative transfer inversion methods similar to those employed for Jupiter (*2*, *4*). Measurements in the 200- to 600-$cm^{-1}$ region, where absorption by $H_2$ is dominant, provide information on the thermal structure between approximately 70 and 700 mbar, while data from the $Q$ branch of the 1304-$cm^{-1}$ $CH_4$ band are sensitive to the temperature within a broad atmospheric layer centered near 1 mbar. Because of the low temperatures in the Saturnian stratosphere, the signal-to-noise ratio at 1304 $cm^{-1}$ does not permit use of the $CH_4$ band for retrieval of profiles from individual spectra; however, useful information can be obtained from averages of several tens of spectra. In obtaining the preliminary retrievals discussed in this report, possible contributions to the atmospheric opacity by haze and clouds have been ignored.

Figure 3 shows two examples of retrieved Saturn profiles and a Jovian profile for comparison. These results were

obtained from zonal averages of approximately 25 spectra. In addition to being substantially cooler, the Saturn profiles show a distinct change in lapse rate near the 400-mbar level which is not observed on Jupiter. The resulting small vertical temperature gradient between 80 and 400 mbar accounts for the relatively low contrast observed in the $S_0$ and $S_1$ $H_2$ lines in the Saturn spectrum. The profile from 13°N, which is typical of the structure observed at low northern latitudes and over much of the southern hemisphere, is essentially in agreement with Pioneer 11 infrared radiometer observations (*6*). However, substantial spatial variations are observed, especially in the northern hemisphere.

Retrieved temperatures for two atmospheric layers, approximately 0.5 scale height thick and centered at 209 and 535 mbar, are plotted as functions of latitude in Fig. 4. The solid curves between 10°S and 65°N represent data acquired from a series of nine north-south scans of 12 to 14 spectra, each with a spatial resolution of 4° to 5° in latitude. The spread in data points about the lines shown is ± 0.5 K, which corresponds to errors expected from instrument noise. Since the individual spectra in the set were acquired over a wide range of longitudes but at the same latitude, the dependence of thermal structure on longitude must be small—unlike the situation on Jupiter, where significant longitudinal variations were found (*12*). The curves at high southern latitudes are from a single north-south scan of 18 spectra, acquired near closest approach with a spatial resolution of about 1.5° in latitude. Also included in Fig. 4 are retrievals of zonal averages from a global mapping sequence with a resolution of about 12°. Data with high spatial resolution were not obtained between 10° and 60°S.

On a global scale, the temperatures at 209 mbar are warmer in the southern than in the northern hemisphere. This is a seasonal effect caused by Saturn's ~ 27° obliquity. The sun crossed the equator into the northern hemisphere in early 1980, but because the radiative time constant at this atmospheric level is comparable to the Saturnian year (*13*), the thermal response is expected to lag behind the seasonal forcing by about one-quarter of the seasonal cycle, resulting in the observed cold northern hemisphere. The measured global scale structure is in agreement with the predictions of Carlson *et al.* (*14*), which are based on the above considerations. Estimates of the radiative time constant at 535 mbar (*15*) indicate a value comparable to that

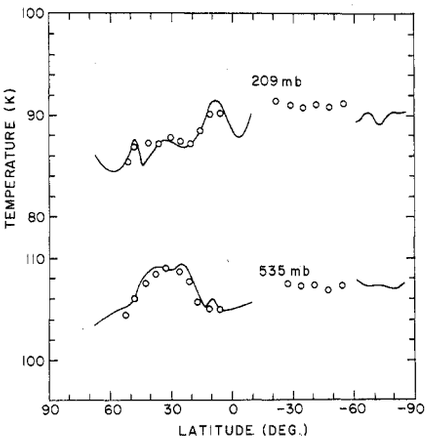


Fig. 4. Retrieved temperatures of Saturn as a function of latitude for the 209- and 535-mbar levels. The curves represent fits to data acquired with a spatial resolution of 4° to 5° in latitude between 10°S and 67°N and a resolution of 1.5° latitude between 60° and 85°S. The open circles represent zonal averages from a global mapping sequence with a resolution of about 12° in latitude.

at 209 mbar; therefore, the observed low temperatures at this level at high northern latitudes (relative to those at high southern latitudes) may also be a seasonal effect. A temperature minimum at 209 mbar between 10° north and south is in agreement with Pioneer 11 observations (*6*). A broader minimum is found at the deeper level between 25° north and south, which is roughly coincident with the high-speed equatorial jet stream inferred from cloud motions in the Voyager images. However, the thermal wind shear of ~ 10 m $sec^{-1}$ per scale height obtained from this latitudinal temperature gradient results in little reduction with altitude of the winds of 400 to 500 m $sec^{-1}$ obtained from imaging observations (*16*). The small spatial scale structure observed in the high-resolution data is well above the noise level of the measurements and is more pronounced than the latitudinal structure observed on Jupiter. On the basis of preliminary analysis, neither the major albedo features of Saturn nor the imaging-derived wind fields appears to be simply correlated with this structure.

*Titan.* The presence of an atmosphere on Titan has been known since 1944, when $CH_4$ was first detected (*17*). Despite substantial progress in recent years in ground-based observation techniques (*18–20*), it has been impossible to discriminate between atmospheric models in which $CH_4$ is the dominant constituent, with a surface pressure only about 20 mbar (*21*), and models in which $N_2$ is the dominant gas, with only small fractions of $CH_4$ and a surface pressure possibly as high as 21 bars (*22, 23*). The Voyager 1 IRIS obtained new information on the composition, structure, and dynamics of Titan's atmosphere. Observations were made from about 8 hours before to 3 hours after closest approach to Titan. To investigate diurnal and latitudinal effects, data were taken from the center of the disk, near the morning and evening limbs at low latitude, and in the polar regions, on both the illuminated and the dark sides.

Figure 5 shows an average of 346 Titan spectra on both radiance and brightness temperature scales. The spectra are

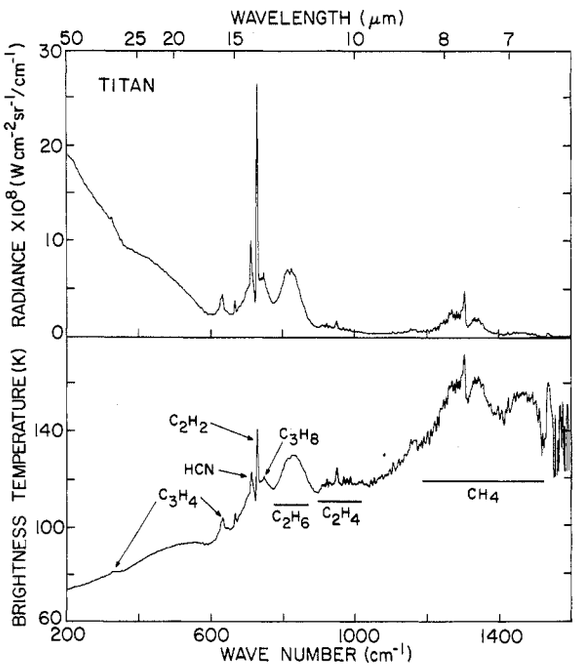


Fig. 5. Average Titan spectrum.

mostly from the center of the disk, but data from latitudes as high as 60° north and south are included. Several strong emission features associated with stratospheric gases are superimposed on a background continuum. Similar behavior is seen in the east limb spectrum taken near the entrance radio occultation point (Fig. 6) (*24*). At low wave numbers the brightness temperature does not level off as expected for a transparent atmosphere but increases with wave number. The minimum brightness temperature of 73 K seen at 200 $cm^{-1}$ imposes an upper limit on the minimum ambient atmospheric temperature because of the trend with wave number and because of the width of the weighting function that governs the emitted radiance. Below 200 $cm^{-1}$, the brightness temperature of Titan cannot decrease much because Titan as a whole must radiate in the infrared, with an effective blackbody temperature of ~ 86 K, in order to balance absorbed sunlight. Consequently, an atmospheric temperature minimum of ~ 70 K seems reasonable.

By combining this information with the scale height profile derived by the radio science investigation (*24*), it is possible to obtain both the vertical temperature profile (Fig. 7) and the mean molecular weight of the atmosphere. The upper portions of the profile in Fig. 7 have been determined from IRIS measurements in the 1304-$cm^{-1}$ $CH_4$ band. A mean molecular weight of about 28 is inferred, suggesting that $N_2$ (or possibly CO) is the dominant atmospheric constituent. Proof that the atmosphere contains nitrogen is provided by the detection of compounds of nitrogen, carbon, and hydrogen by IRIS and the discovery of nitrogen emission by the ultraviolet investigation (*25*). None of the identified atmospheric constituents detected by IRIS contains oxygen, so a predominantly CO atmosphere is not likely.

With the vertical thermal structure known, it becomes feasible to infer the spectral variation of the atmospheric opacity. In the infrared, Titan is spatially homogeneous at low latitudes, without observable diurnal or longitudinal effects; this permits the use of data at different longitudes and hour angles to obtain the variation of radiance with emission angle. Figure 8 shows the wave number dependence of the difference in radiance between emission angles of 52° and 25° divided by the radiance at 25°. Averages of 29 and 102 spectra were used at 52° and 25°, respectively. Limb darkening occurs between 200 and 500 $cm^{-1}$, indicating that thermal emission in this spectral region originates mainly from levels below the atmospheric temperature minimum. Limb brightening for wave numbers greater than 600 $cm^{-1}$ indicates that emission from above the temperature minimum dominates there. Neither limb darkening nor brightening is observed in the plateau between 500 and 600 $cm^{-1}$, where the brightness temperature is approximately 93 K.

Several models have been used to estimate the continuum opacity between 200 and 600 $cm^{-1}$. All models assume the temperature profile shown in Fig. 7 and Beer's law of absorption. Simple models in which the wave number–dependent opacity is proportional to the density reproduce neither the observed limb darkening nor the brightness temperature at 200 $cm^{-1}$. More complex two-layer models do reproduce observed brightness temperatures and limb darkening. They yield opacities in the stratospheric layer which are about two orders of magnitude lower than those in the tropospheric layer. The optical thicknesses between 500 and 600 $cm^{-1}$ calculated for the lower layer are less than 0.1; at these wave numbers Titan's atmosphere must be nearly transparent.

Between 500 and 200 $cm^{-1}$ the computed opacity increases smoothly and monotonically with decreasing wave number in a manner qualitatively similar to that expected for pressure-induced $N_2$ and $CH_4$ absorption. Models with opacities varying as the square of the density, when fitted to the observed radiances,

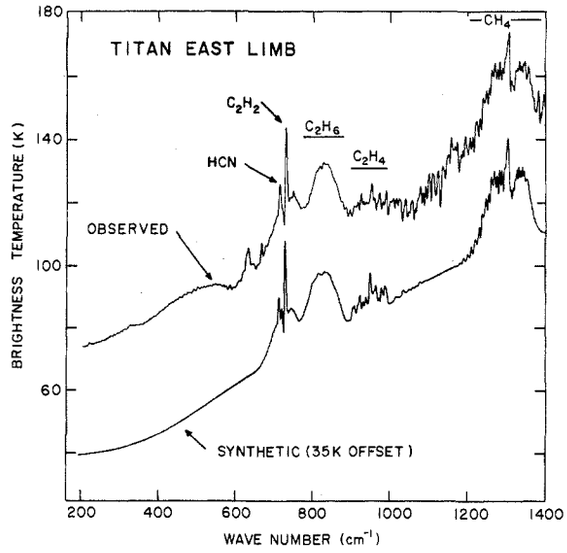


Fig. 6. Equatorial Titan spectrum and calculated comparison spectrum. Most of the strong emission features are due to the minor stratospheric constituents $CH_4$, $C_2H_2$, $C_2H_4$, $C_2H_6$, and HCN.

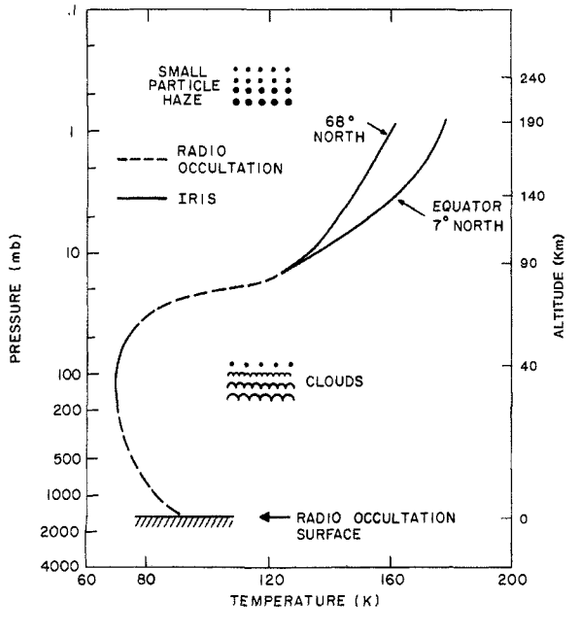


Fig. 7. Temperature profile of Titan. The solid curves are from IRIS data and the dashed parts are from the profile of the temperature–molecular weight ratio obtained by the Voyager radio science investigation. Haze and condensation zones are indicated schematically.

yield total atmospheric optical thicknesses ranging from $< 0.1$ at 600 $cm^{-1}$ to $\sim 25$ at 200 $cm^{-1}$. Calculated and observed limb functions agree to better than 30 percent, implying that these models may be viable alternatives to discrete layer models. Thus, pressure-induced absorption may contribute to the opacity in this spectral region. Scaling the $N_2$ absorption estimated by McCarthy *et al.* (*20*) to Titan implies an optical thickness of $\sim 2$ at 300 $cm^{-1}$, compared with one of $\sim 3$ obtained by fitting the density-squared opacity model to our data. The agreement is suggestive, but other evidence (*26*) indicates that the $N_2$ opacity value proposed by McCarthy *et al.* may be too high.

Another explanation of the opacity increase at low wave numbers is absorption by methane clouds. Data from Savoie and Fournier (*27*) and Obriot *et al.* (*28*) indicate the existence of a strong absorption feature in solid and liquid methane between 120 and 180 $cm^{-1}$; the exact spectral position depends on temperature. From the centers of these features, the opacity decreases slowly and monotonically toward higher wave numbers. Since the tropopause of Titan is probably saturated with $CH_4$, the occurrence of methane clouds would appear inevitable; however, temperatures are too high for $N_2$ condensation. Further work on the opacity of both solid and liquid $CH_4$ in the 100- to 600-$cm^{-1}$ range is needed. Until then we can only speculate that intrinsic absorption in methane haze may contribute to the atmospheric opacity at low wave numbers in a manner that resembles pressure-induced transitions in $N_2$ and $CH_4$. Both effects may be required to explain the measured spectra quantitatively.

Earth-based observations have detected $CH_4$ (*17*), $C_2H_6$ (*19*), $C_2H_2$ (*18, 19*), and possibly $C_2H_4$ (*19*). In the IRIS spectrum shown in Fig. 6 we see the $\upsilon_5$ $C_2H_2$ rotation-vibration band centered at 729 $cm^{-1}$, the broad $\upsilon_9$ band of $C_2H_6$ centered at 821 $cm^{-1}$, and the $\upsilon_7$ band of $C_2H_4$ centered at 950 $cm^{-1}$. In addition to these hydrocarbons, the organic compound HCN has been identified with the emission feature at 712 $cm^{-1}$.

The observed spectrum and the equatorial temperature profile illustrated in Fig. 7 have been used to determine the hydrocarbon concentrations. The models assume a constant mixing ratio down to approximately 50 mbar, where condensation is likely to begin. The most abundant hydrocarbon after $CH_4$ is $C_2H_6$ with a mole fraction of $2 \times 10^{-5}$, followed by $C_2H_2$ with a fraction of $3 \times 10^{-6}$ and $C_2H_4$ with a fraction of $1 \times 10^{-6}$.

In Fig. 9 the measured spectrum of Titan is compared with a computed spectrum that includes HCN. The figure also shows the computed transmittance of 20 cm-atm of HCN at 100 K. Although HCN has been observed in interstellar space (*29*), this is the first observation in a planetary atmosphere. The detection of this organic compound is of considerable interest, since HCN is a key intermediate in the synthesis of amino acids and bases present in nucleic acids. We do not suggest that conditions on Titan are suitable for life; however, we do note that the chemical processes leading to the formation of organic molecules, precursors of biologically important compounds, appear to have occurred on Titan as well as Earth.

The production of HCN in Titan's atmosphere is possible through two types of processes: nitrogen and methane photochemistry and energetic particle bombardment. The possibility of the production of HCN by photolysis of methane in the presence of large concentrations of $N_2$ has been proposed (*30*), and simulation experiments with ultraviolet radiation on a mixture of methane and ammonia have produced a number of organic compounds, including HCN (*31*). A pre-Voyager summary of the production of organics, including HCN, by energetic particle bombardment was made by Chang *et al.* (*32*). A post-Voyager suggestion by Strobel (*33*) identifies significant HCN production from both electron bombardment and solar ultraviolet radiation.

Figure 10 illustrates the striking differences between some features in the north polar and mid-latitude spectra. The polar spectrum (an average of 30 individual spectra) was recorded at high spatial resolution at 68°N (emission angle $\sim 63°$) near or on the dark polar hood observed in Voyager images (*16*). The east limb spectrum is the average of 29 spectra recorded at a slightly lower spatial reso-

Table 2. Atmospheric composition of Titan.

| Gas | Band | Wave number ($cm^{-1}$) | Approximate mole fraction |
|---|---|---|---|
| Positively identified | | | |
| Methane ($CH_4$) | $\upsilon_4$ | 1304 | $1 \times 10^{-2}$ |
| Ethane ($C_2H_6$) | $\upsilon_9$ | 821 | $2 \times 10^{-5}$ |
| Acetylene ($C_2H_2$) | $\upsilon_5$ | 729 | $3 \times 10^{-6}$ |
| Ethylene ($C_2H_4$) | $\upsilon_7$ | 950 | $1 \times 10^{-6}$ |
| Hydrogen cyanide (HCN) | $\upsilon_2$ | 712 | $2 \times 10^{-7}$ |
| Tentatively identified | | | |
| Methylacetylene ($C_3H_4$) | $\upsilon_9$, $\upsilon_{10}$ | 633, 328 | |
| Propane ($C_3H_8$) | $\upsilon_{26}$ | 748 | |

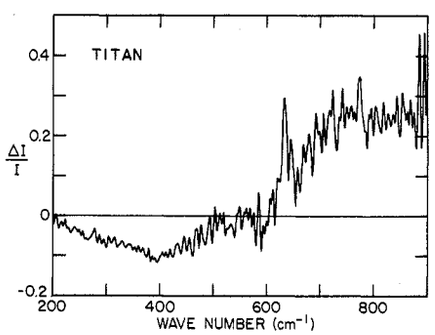


Fig. 8. Low-latitude spectral limb function of Titan (emission angles 52° and 25°). The intensity ratio $\Delta I/I$ is $[(I(52°) - I(25°)]/I(25°)$. Negative values indicate that the emission originates below the atmospheric temperature minimum and positive values indicate stratospheric emission.

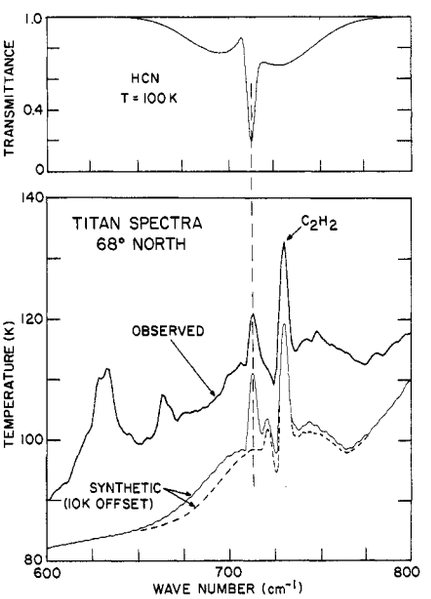


Fig. 9. Hydrogen cyanide on Titan. A north polar spectrum of Titan is compared with a synthesized spectrum in which only $C_2H_2$, $C_2H_6$, and HCN have been included. The feature at 720 $cm^{-1}$ in the synthetic spectrum is an artifact. A computed absorption spectrum (20 cm-atm at 100 K) is shown for comparison.

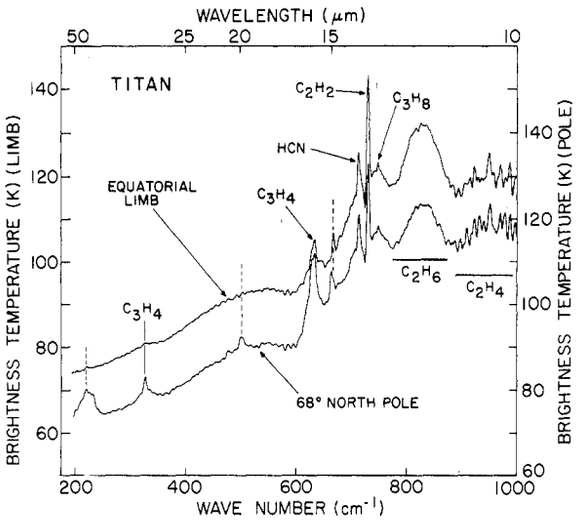


Fig. 10. Comparison of north polar and equatorial Titan spectra. Unidentified features are marked by dashes. The upper curve is an average of 30 north polar spectra with emission angles of 63° and the lower curve is an average of 29 east limb spectra with emission angles at 45°. For clarity the spectra have been shifted by 10 K, as indicated by the vertical temperature scales. The striking differences may be associated with the north polar hood.

lution at a latitude of ~ 7° and an emission angle of ~ 45°. Some of the differences may therefore be attributed to different emission angles, but others are clearly of thermal and compositional origin. Despite the lower temperatures in the northern stratosphere (Fig. 7), many spectral features are markedly enhanced in the north compared to those at midlatitudes. It is tempting to link these features with chemical processes also responsible for the north polar hood.

In Fig. 10 the spectral features at 328 and 633 $cm^{-1}$ have tentatively been assigned to methylacetylene ($C_3H_4$) and the feature at 748 $cm^{-1}$ to propane ($C_3H_8$). The molecular identifications are summarized in Table 2. Additional laboratory spectroscopy and atmospheric modeling are necessary to verify the tentative identifications and to allow assignments to other unidentified features.

The hydrocarbon concentration on Titan is substantially higher than on Jupiter and Saturn. The Titan/Saturn ratio for $C_2H_6$ is ~ 4 and for $C_2H_2$ ~ 150. So far, $C_2H_4$ has not been detected on either Jupiter or Saturn. The higher hydrocarbon abundances on Titan are a consequence of the high escape rate of H, which prevents rapid recycling of $CH_4$ by the reaction $H + CH_3 + M \rightarrow CH_4 + M$. On Titan more than 95 percent of the dissociated $CH_4$ is irreversibly converted to $C_2H_2$ and $C_2H_6$ (*34*). The constant removal of $CH_4$ from the upper atmosphere by chemical reactions requires a replenishment of $CH_4$ from the surface. The 70 K temperature minimum at 200 mbar acts as a cold trap for $CH_4$ and any other minor constituent whose source lies below this level. The stratospheric mole fraction of $CH_4$ is thereby limited to about 0.01 (*35*), corresponding to saturation at the tropopause. The tropopause thus regulates and maintains a constant abundance of stratospheric $CH_4$ on Titan, much as it does for stratospheric water vapor on Earth. Although gases produced photochemically or through charged particle impact in the stratosphere can have concentrations in excess of saturation at the tropopause, they will condense and precipitate as they are transported downward.

The IRIS data indicate no longitudinal contrasts. Stratospheric temperatures near 1 mbar are approximately 20 K colder in the north than at equatorial and southern latitudes (see Fig. 7). Deeper in the atmosphere, meridional contrasts are much smaller. Although at the deeper levels of Titan's atmosphere the sources of infrared opacity have not all been identified, the 1304-$cm^{-1}$ band of $CH_4$ probably represents the major source of opacity at 1 mbar. The calculations of Cess and Caldwell (*13*), when scaled to Titan, imply a radiative damping time of approximately 3 years at this level, which is long compared to Titan's diurnal period (16 days) and consistent with the observed axisymmetric thermal structure. The radiative damping time is comparable to the seasonal time scale and is consistent with a meridional thermal structure that lags in phase behind the seasonally varying solar heating. At the time of the encounter, the subsolar point had just moved into Titan's northern hemisphere. Scaling considerations (*13*, *14*) suggest a global contrast of 20 K from radiative effects alone. Thus the thermal structure of Titan's stratosphere may be radiatively controlled, although the possibility of some dynamic effects cannot be excluded. The reduced thermal contrasts in the troposphere suggest a longer radiative damping time and efficient dynamic transport of energy.

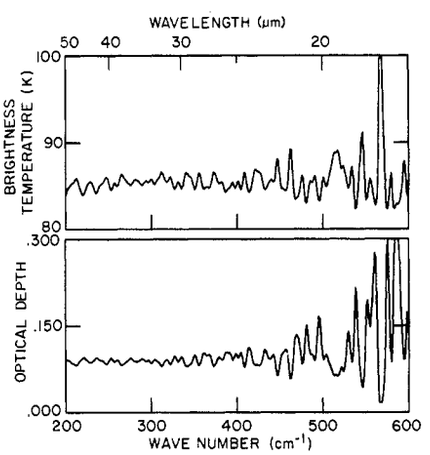


Fig. 11. Temperature and optical depth of the C ring. The temperature and the optical depth normal to the ring plane were computed from a combined analysis of spectra recorded at different emission angles. Each spectral data point represents an independent measurement.

The observed thermal contrast at 1 mbar implies the existence of a meridional gradient in geopotential, which must be dynamically balanced. One possibility, originally suggested by Gierasch *et al.* (*36*) and Stone (*37*) for the deep circulation in the atmosphere of Venus, is the formation of a Hadley cell with little zonal flow, in which the meridional gradient in geopotential is balanced by the advection of northward momentum. However, such a circulation is very efficient in the transport of heat and would yield a thermal contrast in Titan's stratosphere several orders of magnitude less than that observed. It is more plausible that the meridional gradient in geopotential is balanced by a cyclostrophic zonal flow, as is the case in Venus's stratosphere (*38*). Integrating the cyclostrophic balance equation from 1000 to 1 mbar by using the horizontal temperature contrasts given in Fig. 7 yields zonal wind speeds of ~ 100 m $sec^{-1}$, which is ten times Titan's equatorial surface speed (assuming Titan's rotation equals its orbital period). If the horizontal gradients occur over scales less than the planetary radius, larger wind speeds are implied. The difficulties in maintaining a superrotating atmosphere have been extensively studied for Venus (*39*). However, Titan's stratosphere differs from that of Venus in two important respects: diurnal effects are absent on Titan, and its stratospheric structure changes with season, implying concomitant shifts in latitude of the superrotating zonal flow.

*Rings*. A pair of observations made 2 hours apart have been used to determine the temperature and opacity of a portion

of the C ring. Centered at 1.40 Saturn radii, the instrument footprint decreased from one-quarter to one-eighth of the annular width of the ring between the observations; in the same interval, the emission angle decreased from 85.8° to 82.6°. If scattering is ignored, the observed intensity from the ring may be written $I(\upsilon) = B(\upsilon,T)(1-e^{-\tau(\upsilon)\sec\theta})$, where $I(\upsilon)$ and $\tau(\upsilon)$ are the observed radiance and the optical depth normal to the ring, respectively, as functions of wave number $\upsilon$; $B(\upsilon,T)$ is the Planck function; $T$ is the ring temperature; and $\theta$ is the emission angle, measured from the ring-plane normal. The derived temperature, 85 ± 1 K, and the optical depth of the ring, 0.09 ± 0.01, are shown in Fig. 11. They are quite consistent with the values obtained by Froidevaux and Ingersoll (*40*) from Pioneer data. The lack of an increase in opacity with wave number indicates that the ring cross section is not dominated by particles with radii of the order of 1 μm.

Diagnostic spectral features of such components as water ice, with an absorption near 227 $cm^{-1}$, and silicates, many of which have SiO bending modes between 400 and 500 $cm^{-1}$, are absent from the spectrum. If either of these materials is present in the ring, this lack of features is also consistent with the absence of a dominant fraction of micrometer-sized particles. A similar lack of spectral features in the thermal infrared was observed for Europa (*2*), although the satellite is almost entirely covered with water ice. The absence of an infrared signature is due to the low thermal contrast established across the

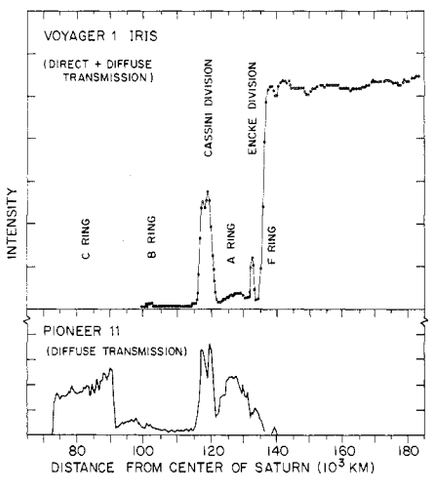


Fig. 12. Transmission measurement of Saturn's rings. Solar radiance was measured through the 20° off-axis calibration port of IRIS as the rings occulted the sun. Pioneer data for diffuse transmission are shown for comparison.

Table 3. Preliminary brightness temperature estimates for the A, B, and C rings.

| Ring | Brightness temperature (K) | |
|---|---|---|
| | Unilluminated side | Illuminated side |
| A | 50 to 60 | |
| B | >50 | 70 to 75 |
| C | 85 | |

porous surface layer. This, in turn, suggests that a "regolith" exists on the ring particles.

Additional information on the C ring particles was obtained from two observations of the passage of ring material into the planetary shadow. An observation at low phase angle showed a drop in temperature as the particles passed from light to dark (determination of the actual cooling rate requires pointing data that are not yet available). A similar observation at high phase angle showed a nearly constant low temperature under the same conditions. This indicates that the ring particle size distribution is not dominated by particles less than a few millimeters in size and that the particles are not rapidly rotating.

Table 3 summarizes preliminary brightness temperatures for the illuminated and unilluminated sides of the classical rings. Except for the C ring data, these data are uncorrected for optical depth and the geometry of the observations, and so represent lower limits to actual temperatures. All the results appear consistent with values obtained from Pioneer (*40*).

Following occultation of the sun by the planet, additional ring data were obtained by viewing the sun as it was occulted by the rings. The observation, made with the off-axis calibration port of IRIS (1.6° diameter field of view), began when the sun was behind the B ring and extended until it was well beyond the F ring; the data, taken from the radiometer channel, are shown in Fig. 12. The Cassini division, Encke division, and F ring are all apparent. Comparison of the observations with those from the Pioneer 11 photopolarimeter (*41*) shows good agreement. The apparent reversal of features in the Encke division and the F ring is due to the difference between direct transmission (IRIS) and diffuse transmission (Pioneer) in these optically thin regions. The structure outside the F ring must be carefully scrutinized; pointing offsets which place the sun near the edge of the instrument field of view could cause spurious intensity changes. Analysis of the data is further complicated because the projection of the sun in the rings is greater than the width of the Cassini division. With estimated uncertainties on the order of a factor of 2, the normal optical depth of the Cassini division is 0.05; assuming that the data are not contaminated by pointing difficulties, the normal optical depth near 160,000 km is $2 \times 10^{-3}$.

*Rhea.* Observations of the Saturnian satellites by IRIS were limited by the small sizes of the objects and the rather large encounter distances. Only Rhea was observed with substantially better than disk resolution.

The brightness temperature and the physical temperature of a surface element on a smooth, slowly rotating planetary body is given by

$$T(\theta) = \frac{T_0}{R^{1/2}} \left(\frac{1-A}{\epsilon}\right)^{1/4} \cos^{1/4}\theta$$

where $A$ is the bolometric bond albedo, $\epsilon$ is the radiometric emissivity, $R$ is the distance from the sun in astronomical units, and $\theta$ is the solar zenith angle. $T_0$ is normally 395 K, the blackbody equilibrium temperature at the Earth's distance from the sun, but observations of the moon have shown that a better estimate is 400 K because of peaking of the infrared emissivity at small phase angles (*42*). Thermal observations of asteroids and other planetary satellites suggest that $T_0$ may be as high as 408 K.

At a solar phase angle of 15°, the brightness temperature measured near the subsolar point of Rhea was 99 ± 2 K. Assuming unit emissivity, this gives a bolometric (spectrally averaged) bond albedo of 0.67 ± 0.03. The bolometric geometric albedo of Rhea from ground-based photometry, combined with the radius of the satellite derived from Voyager images, is $p_{bol} = 0.65 \pm 0.02$. The phase integral is therefore $q = A_{bol}/p_{bol} = 1.02 \pm 0.06$, where the error es-

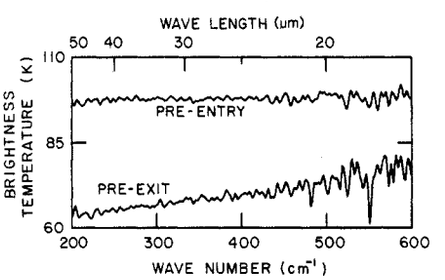


Fig. 13. Rhea eclipse temperatures. The brightness temperatures of Rhea are shown before entry into Saturn's shadow and before leaving it. The slope of the pre-exit curve indicates a range of surface temperatures caused by a range of thermal inertia values of the material on Rhea's surface.

timate reflects the uncertainties of 0.02 in $P_{bol}$, 2 K in the measured temperature and 6 K in $T_0$ in the above equation. This value of $q$ is in good agreement with that determined for other icy bodies; Morrison (*43*) found $q = 1.0 \pm 0.2$ and $1.0 \pm 0.3$ for Europa and Ganymede, respectively. These high values are distinctly different from 0.6, which is typical of rocky objects of low geometric albedo, such as the moon.

The observed brightness temperatures across the surface of Rhea indicate that the thermal emission is peaked in the backward direction. A mosaic of nine temperature measurements was obtained when the solar phase angle was 15°; subsequently, some of the same surface was observed with comparable spatial resolution but at a solar phase angle of 77°. The central regions of the disk seen at the approach give $T = 99 \pm 2$ K, with a gradual decrease to $93 \pm 2$ K at the extreme limbs and poles. Seen from the high angle view, the same high latitudes give $T = 83 \pm 4$ K, while at low latitudes $T = 90 \pm 4$ K.

An anisotropy in the emissivity of the moon has been attributed to the large- and small-scale roughness (*44*). Because, at a topographic scale of a few kilometers, Rhea and the moon are quite similar as judged from the Voyager images (*16*), we presume that the same situation applies to the emission properties of both bodies. The geometric albedo of Rhea is greater than that of the moon by a factor of ~ 9 because it is composed predominantly of ice, and it therefore appears that, to a first approximation, the geometric emission properties of solar system bodies without atmospheres are independent of composition and albedo.

A disk observation of Rhea in eclipse was also obtained; relative to an observation made before eclipse entry, the disk flux dropped by about 75 percent. The brightness temperature spectra of the observation are shown in Fig. 13. The nearly wave number–independent pre-eclipse brightness temperature of $96 \pm 2$ K is consistent with the spatially resolved measurements discussed above. The significant slope in brightness temperature measured in eclipse indicates lateral inhomogeneities in the surface thermal properties of the satellite. Decomposition of the spectrum (assuming a mixture of two surface temperatures) indicates that roughly half the surface cools to about 75 K, while the remainder cools to less than 55 K. This indicates the presence of components having high and low thermal inertia. The high inertia component is probably solid material with a block size comparable to or greater than the thermal skin depth $\sqrt{\tau K/\pi\rho C}$ (where $\tau$ is the period of the insolation change and $K$, $\rho$, and $C$ are the thermal conductivity, density, and heat capacity of the material). For the eclipse observation, assuming the material to be water ice, the thermal skin depth ≃ 10 cm. The low inertia component is most likely a thin frosty layer, such as is present on Europa and Ganymede.


R. HANEL
B. CONRATH
F. M. FLASAR
V. KUNDE
W. MAGUIRE
J. PEARL
J. PIRRAGLIA
R. SAMUELSON
L. HERATH

*Goddard Space Flight Center, Greenbelt, Maryland 20771*

M. ALLISON

*Rice University, Houston, Texas 77001*

D. CRUIKSHANK

*University of Hawaii, Honolulu 96822*

D. GAUTIER

*Paris Observatory Meudon, France*

P. GIERASCH

*Cornell University, Ithaca, New York 14853*

L. HORN
R. KOPPANY

*Jet Propulsion Laboratory, Pasadena, California 91109*

C. PONNAMPERUMA

*University of Maryland, College Park 20742*


### References and Notes


1. R. Hanel, D. Crosby, L. Herath, D. Vanous, D. Collins, H. Creswick, C. Harris, M. Rhodes, *Appl. Opt.* **19**, 1391 (1980).
2. R. Hanel, B. Conrath, M. Flasar, V. Kunde, P. Lowman, W. Maguire, J. Pearl, J. Pirraglia, R. Samuelson, D. Gautier, P. Gierasch, S. Kumar, C. Ponnamperuma, *Science* **204**, 972 (1979); R. Hanel, B. Conrath, M. Flasar, L. Herath, V. Kunde, P. Lowman, W. Maguire, J. Pearl, J. Pirraglia, R. Samuelson, D. Gautier, L. Horn, S. Kumar, C. Ponnamperuma, *ibid.* **206**, 952 (1979); J. Pearl, R. Hanel, V. Kunde, W. Maguire, K. Fox, S. Gupta, C. Ponnamperuma, F. Raulin, *Nature (London)* **280**, 755 (1979); S. Kumar, *ibid.*, p. 758; R. Hanel *et al.*, *J. Geophys. Res.*, in press; D. Gautier *et al.*, in (*5*); B. J. Conrath *et al.*, *ibid.*, in press; F. M. Flasar *et al.*, *ibid.*, in press; G. E. Hunt, B. J. Conrath, J. A. Pirraglia, *ibid.*, in press.
3. R. Wildt, *Naturwissenchaften* **20**, 851 (1932); G. Münch and H. Spinrad, *Monogr. Soc. R. Sci. Liège Ser. 5* **7**, 541 (1963); L. P. Giver and H. Spinrad, *Icarus* **5**, 586 (1966); F. Gillett and W. Forrest, *Astrophys. J.* **187**, L37 (1974); A. Tokunaga, R. F. Knacke, T. Owen, *ibid.* **197**, L77 (1975); J. D. Bregman, D. F. Lester, D. M. Rank, *Astrophys. J. Lett.* **202**, L55 (1975); H. P. Larson, U. Fink, H. A. Smith, D. S. Davis, *Astrophys. J.* **240**, 327 (1980).
4. B. J. Conrath and D. Gautier, in *Remote Sensing of Atmospheres and Oceans*, A. Deepak, Ed. (Academic Press, New York, 1980), p. 611; D. Gautier and K. Grossman, *J. Atmos. Sci.* **29**, 788 (1972).
5. D. Gautier, B. Conrath, M. Flasar, R. Hanel, V. Kunde, A. Chedin, M. Scott, *J. Geophys. Res.*, in press.
6. G. S. Orton and A. P. Ingersoll, *ibid.* **85**, 5871 (1980); A. P. Ingersoll, G. S. Orton, G. Münch, G. Neugebauer, S. C. Chase, *Science* **207**, 439 (1980).
7. D. J. Stevenson and E. E. Salpeter, *Astrophys. J. Suppl. Ser.* **35**, 239 (1977).
8. D. J. Stevenson, *Science* **208**, 746 (1980).
9. J. B. Pollack, A. S. Grossman, R. Moore, H. C. Graboske, Jr., *Icarus* **30**, 111 (1977); A. S. Grossman *et al.*, *ibid.* **42**, 358 (1980).
10. H. H. Kieffer, *J. Geophys. Res.* **72**, 3179 (1967); F. M. Flasar, *Astrophys. J.* **186**, 1097 (1973).
11. D. L. Harris, in *Planets and Satellites*, G. P. Kuiper and B. M. Middlehurst, Eds. (Univ. of Chicago Press, Chicago, 1961), p. 306.
12. G. E. Hunt, B. J. Conrath, J. A. Pirraglia, *J. Geophys. Res.*, in press.
13. R. D. Cess and J. Caldwell, *Icarus* **38**, 349 (1979).
14. B. E. Carlson, J. Caldwell, R. D. Cess, *J. Atmos. Sci.* **37**, 1883 (1980).
15. P. J. Gierasch and R. M. Goody, *ibid.* **26**, 979 (1969).
16. B. A. Smith, L. Soderblom, R. Beebe, J. Boyce, G. Briggs, A. Bunker, S. A. Collins, C. J. Hansen, T. V. Johnson, J. L. Mitchell, R. J. Terrile, M. Carr, A. F. Cook II, J. Cuzzi, J. B. Pollack, G. E. Danielson, A. Ingersoll, M. E. Davies, G. E. Hunt, H. Masursky, E. Shoemaker, D. Morrison, T. Owen, C. Sagan, J. Veverka, R. Strom, V. E. Suomi, *Science* **212**, 163 (1981).
17. G. P. Kuiper, *Astrophys. J.* **100**, 378 (1944).
18. A. Tokunaga, *Bull. Am. Astron. Soc.* **12**, 669 (1980).
19. F. C. Gillett, F. J. Low, W. A. Stein, *Astrophys. J.* **157**, 925 (1969).
20. J. F. McCarthy *et al.*, *ibid.* **236**, 701 (1980).
21. R. E. Danielson *et al.*, *Icarus* **20**, 437 (1973); J. Caldwell, in *Planetary Satellites*, J. A. Burns, Ed. (Univ. of Arizona Press, Tucson, 1977), p. 438.
22. D. M. Hunten, in *Planetary Satellites*, J. A. Burns. Ed. (Univ. of Arizona Press, Tucson, 1977), p. 420.
23. S. K. Atreya, T. M. Donahue, W. R. Kuhn, *Science* **201**, 611 (1978).
24. G. L. Tyler, V. R. Eschleman, J. D. Anderson, G. S. Levy, G. F. Lindal, G. E. Wood, T. A. Croft, *ibid.*, **212**, 201 (1981).
25. A. L. Broadfoot *et al.*, *ibid*, p. 206.
26. R. Courtin, personal communication; K. Fox, personal communication.
27. R. Savoie and R. P. Fournier, *Chem. Phys. Lett.* **7**, 1 (1970).
28. J. Obriot, F. Fondère, P. Marteau, H. Vu, K. Kobashi, *ibid.* **60**, 90 (1978).
29. L. E. Snyder and D. Buhl, *ibid.* **163**, L47 (1971).
30. A. H. Laufer and A. M. Bass, *Combust. Flame* **32**, 215 (1978).
31. F. Raulin, A. Bossard, G. Toupance, C. Ponnamperuma, *Icarus* **38**, 358 (1979).
32. S. Chang, T. Scattergood, S. Arnowitz, J. Flores, *Rev. Geophys. Space Phys.* **17**, 1923 (1979).
33. D. F. Strobel, *Geophys. Res. Lett.*, in press.
34. ——— *Icarus* **21**, 466 (1974).
35. R. D. Goodwin, *J. Res. Natl. Bur. Stand. Sect. A* **74**, 655 (1970).
36. P. J. Gierasch, R. M. Goody, P. H. Stone, *Geophys. Fluid Dyn.* **1**, 1 (1970).
37. P. H. Stone, *J. Atmos. Sci.* **31**, 1681 (1974).
38. C. B. Leovy, *ibid.* **30**, 1218 (1973).
39. P. H. Stone, *ibid.* **32**, 1005 (1975); P. J. Gierasch, *ibid.*, p. 1038; R. E. Young and J. B. Pollack, *ibid.* **34**, 1315 (1977); W. B. Rossow and G. P. Williams, *ibid.* **36**, 377 (1979); G. Schubert *et al.*, *J. Geophys. Res.* **85**, 8007 (1980).
40. L. Froidevaux and A. P. Ingersoll, *J. Geophys. Res.* **85**, 5929 (1980).
41. T. Gehrels *et al.*, *Science* **207**, 434 (1980).
42. J. M. Saari, R. W. Shorthill, D. F. Winter, *Moon* **5**, 179 (1972).
43. D. Morrison, in *Planetary Satellites*, J. A. Burns, Ed. (Univ. of Arizona Press, Tucson, 1977), p. 269.
44. T. J. Jones and D. Morrison, *Astrophys. J.* **79**, 892 (1974).


45. We thank D. Jennings, J. Heaney, and K. Stewart for recording the infrared spectra of various hydrocarbons; A. Maki for generating the HCN molecular parameters; E. Gardner, S. Gupta, R. Khanna, and E. Ochiaii for laboratory studies, including particle bombardment of mixtures of $N_2$ and $CH_4$; K. Fox for methane parameters; D. Collins for engineering support; and J. Hornstein, L. Mayo, J. Tingley, and J. Frost for data-processing support.

9 February 1981